PCCP

Interlayer expansion process of octacalcium phosphate by forcing the oxidation of intercalated molecules during phase conversion

Journal:	*Physical Chemistry Chemical Physics*
Manuscript ID	CP-ART-05-2023-001992.R3
Article Type:	Paper
Date Submitted by the Author:	16-Aug-2023

Complete List of Authors:	Sugiura, Yuki; National Institute of Advanced Industrial Science and Technology, Health Research Institute Yamada, Etsuko; AIST Horie, Masanori; National Institute of Advanced Industrial Science and Technology (AIST),

Interlayer expansion of octacalcium phosphate via forced oxidation of the intercalated molecules within its interlayers

Received 00th January 20xx,
Accepted 00th January 20xx

DOI: 10.1039/x0xx00000x

Yuki Sugiura,*[a,b] Etsuko Yamada [a] and Masanori Horie [a]

Octacalcium phosphate (OCP), a precursor to apatite, has a layered structure that allows various molecules to be intercalated within its interlayers. Previous research on the phase conversion process of OCP to apatite indicated that the layered structures typically collapse due to shrinking of the OCP layers. In contrast, this study presents a novel phenomenon involving OCP layer expansion during phase conversion. This expansion is based on a forced oxidation process of the intercalated molecules within the hydrous layers of OCP. By introducing NaClO to an OCP interlayer containing dithiodiglycolic acid (DSG), the OCP layers expanded. The process involves DSG decomposition through its reaction with NaClO. Specifically, the process occurs when a DSG-substituted OCP (containing disulfide bonds (–S–S–)) is immersed in a NaClO solution. This is the first study to report the expansion phenomenon during the phase conversion process from OCP to apatite, providing a new perspective to the conventional understanding that these layers only shrink.

Introduction

Global energy and environmental challenges have prompted considerable interest in the development of new carrier materials for catalysts, batteries, and adsorbents through ecofriendly chemical processes. Layered materials and calcium phosphates are considered key materials for solving current social problems. Layered materials, such as mica, clay minerals, layered double hydroxides, and MoS_2, exhibit strong two-dimensional in-plane chemical bonds with only weak bonds, such as van der Waals bonds, along the *a*-axis, which enables the incorporation of targeted molecules between the material layers.[1-5] Moreover, they serve as an attractive basis for smart materials for switchable processes.

Calcium phosphate is the main inorganic component of vertebrate hard tissues. It exhibits excellent biocompatibility and low environmental loading.[6-9] Based on these properties, it is widely used as biomaterials and catalytic supports for light-curing catalysts.[10-13]

Octacalcium phosphate [OCP: $Ca_8(HPO_4)_2(PO_4)_4{\cdot}5H_2O$] is an only layered compound of calcium phosphate.[14-16] OCP exhibits the advantages of a layered structure and those of calcium phosphate. Various molecules, such as cations, dicarboxylic acids, ammonium, tris(hydroxyl) amino methane, and silicas, can be incorporated into OCP through replacing the hydrous layer of OCP unit lattice.[17-26] Based on these mechanisms, new combinations of drug biomaterials were fabricated using OCP units as drug capsules.[17,27,28]

Although the molecular substitution in the OCP unit lattice is well investigated, the releasing process of the substituted molecules from the interlayer of OCP is still unclear. Yokoi et al.[29] suggested that when OCP with substituted dicarboxylic acid molecules (OCP–COOH) is immersed in water under hydrothermal conditions, OCP-COOH is converted to apatite through releasing the substituted molecules from the interlayer via the same mechanism as conventional OCP. This process also suspended our previous studies using OCP–COOH and basic phosphate solutions under basic conditions.[30] Note that large, substituted cations were also replaced with other cations with ionic radii that are closer to Ca^{2+}.[31,32]

The study of the OCP layer expansion process during the molecule releasing process is valuable for engineering and solid-state physics because it acts as a basis for the development of new catalyst suspenders and molecule sieves. Up to now, previous studies only indicated the layer shrinkage process of molecule-substituted OCP during both the releasing process of the substituted molecule and the phase conversion process.[21,29-31,33-35] In this study, the effects of forced oxidation of the substituted molecules on the physicochemical properties of OCP were explored using dicarboxylic acid dithiodiglycolic acid [(DSG): $HOOC\text{-}CH_2\text{-}S\text{-}S\text{-}CH_2\text{-}COOH$] containing disulfide bonds (–S–S–). We hypothesized that the decomposition of the interlayer-immobilized disulfide molecules could generate novel materials and physicochemical phenomena during the phase conversion process. This study deviates from the conventional gradual detachment process of the substituted molecules and instead proposes a rapid and efficient molecular reaction process for swiftly controlling the properties of the substituted materials.

Materials and method

Preparation of DSG-substituted OCP: Layer expansion process

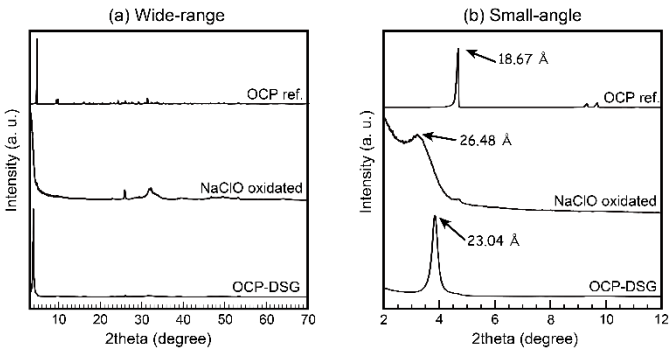

Fig. 1. XRD patterns of OCP-DSG and NaClO-oxidated OCP-DSG. (a) Wide-range. (b) Small-angle.

[a] *Health and Medical Research Institute, National Institute of Advanced Industrial Science and Technology (AIST), 2217-14 Hayashi-cho, Takamatsu, Kagawa, Japan 761-0395.*
[b] *Research Planning Office, Headquarter of Department of Life Science and Biotechnology, National Institute of Advanced Industrial Science and Technology (AIST), 1-1-1 Umezono, Tsukuba, Ibaraki, Japan 305-3305.*
† Corresponding author; Dr. Yuki Sugiura, yuki-sugiura@aist.go.jp

prism made of diamond. We used the surrounding atmosphere

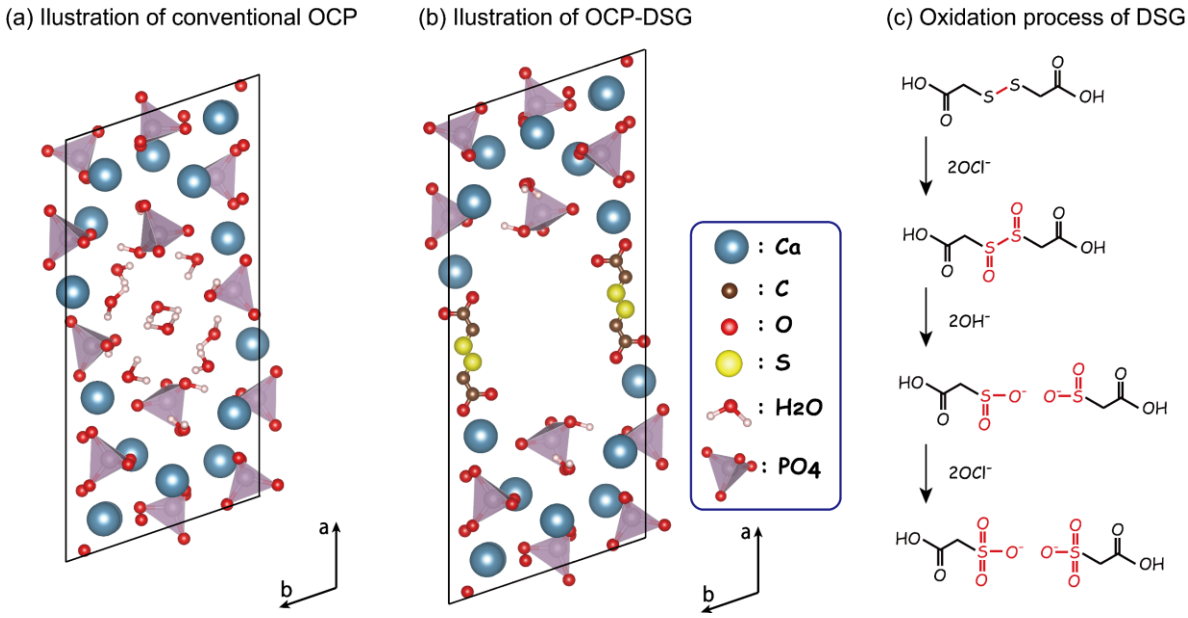

Scheme 1. OCP–DSG oxidation process of NaClO. (a) Schematic of conventional OCP. (b) Plausible schematic of OCP–DSG. (c) Oxidation sequence of DSG using NaClO.[45,46]

$CaCO_3$, H_3PO_4 (85 wt%) and NaClO (25 wt%) were purchased from FUJI Film Wako Pure Chemical Industry Inc., Osaka, Japan. DSG was purchased from Tokyo Kasei Industrial Co., Tokyo, Japan. H_3PO_4 (85 wt%) was diluted using distilled water to achieve a H_3PO_4 concentration of 2.0 mol/L.

DSG (9.0 g) and H_3PO_4 (2.0 mol/L) were diluted using distilled water to yield solutions containing H_3PO_4 and DSG with concentrations of 200 and 100 mmol/L, respectively. $CaCO_3$ powder (20 g) was gradually added to the prepared solution (500 mL). After the initial CO_2 bubbling stabilized, the sample vessels were sealed and incubated at 60°C for 24 h. After the incubation, the samples were repeatedly washed with distilled water before being placed in a dry oven at 40 °C overnight. The NaClO immersion samples were then prepared.

To prevent toxic gas dispersion, the forced oxidation process was conducted under a draft bench. The dried sample powder (1 g) was place in a NaClO solution (25 wt%, 30 mL) and left it at room temperature for 12 h. After oxidation, the samples were repeatedly washed with distilled water and dried in an oven at 40°C overnight.

Characterization

We gathered crystallographic data on the samples using X-ray diffraction (XRD: MiniFlex600, Rigaku Co., Japan) at an acceleration voltage and amplitude of 40 kV and 15 mA, respectively. The diffraction angle was continuously scanned at a rate of 2°/min, with 2 θ values ranging from 3° to 70°. The relative integral intensities of each peak in the obtained XRD patterns were calculated using PDXL2 software (Rigaku Co., Japan) based on the LeBail method.[36]

We analyzed the samples' chemical bonding structure using Fourier transform-infrared spectroscopy (FT-IR: IRTracer-100, Shimadzu Co., Japan). We employed a triglycine sulfate detector (30 scans, resolution 2 cm^{-1}) with an attenuated total reflection as the background for these measurements.

We used field emission-scanning electron microscopy (FE-SEM: JSM-6700F, JEOL Co., Japan) at an acceleration voltage of 3 kV after osmium spattering to analyze the microstructure of the samples.

The samples were dissolved in 2 wt% HNO_3, and their calcium, phosphorus (PO_4), and sodium contents were determined using inductively coupled plasma atomic emission spectroscopy (ICP-OES: 5110VDV, Agilent Technology Co., Japan).

We measured the specific surface areas of the samples using low-temperature nitrogen adsorption (NOVA1200e, Quantachrome Instruments Japan Co., Japan), following the Brunauer–Emmett–Teller (BET) method.[37] The samples were evacuated overnight at room temperature, and nitrogen was introduced in eleven pressure steps (P/P_0 = 0.05–0.90) at −196°C.

The sulfur content of the samples was measured using X-ray fluorescence spectroscopy (XRF: EDX–8100, Shimadzu Co., Japan) at an acceleration voltage of 50 kV under vacuum conditions. The sulfur to calcium ratio was calibrated using a disc-shaped mixture of $CaCO_3$–$CaSO_4 \cdot 2H_2O$ set blocks with fixed ratio.

Finally, the samples were dried using a P_2O_5 desiccator, and their carbon contents were determined through carbon–hydrogen–nitrogen analysis (CHN-analysis: MT-6, Yanaco Co., Kyoto, Japan), using Ar as the carrier gas.

Results and discussions

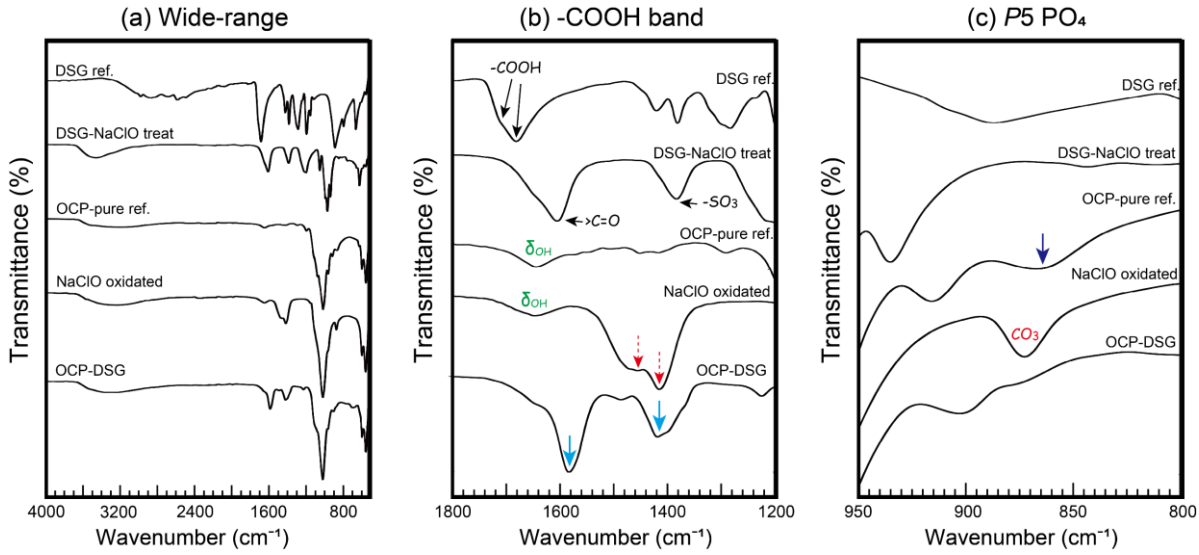

Fig. 2. FT–IR spectra of OCP-DSG and NaClO-oxidated OCP-DSG: (a) Wide range. (b) –COOH band. Light blue arrows: –COOH intercalation within the interlayer of OCP.[19,47,48] Red broken arrows: B-type CO_3 substitute of apatite (CO_3Ap).[38,39] (c) *P*5 PO_4 region. Blue broken line: *P*6 PO_4 vibration.[48] Red arrow: CO_3 adsorption on the apatite surface.[39]

Figure 1 shows the XRD patterns of the samples. Before the oxidation using NaClO, the main peak, i.e., d(100), of the OCP synthesized with DSG shifted to 3.9° from the OCP standard value at 4.7° , indicating that DSG was successfully substituted into the OCP interlayer. Hereafter, we refer to the DSG-substituted OCP as OCP-DSG. The d(100) peak in OCP‐DSG considerably shifted to a lower angle (~3.2°) following the oxidation using NaClO, and the full width at half maximum (FWHM) of this peak notably increased. The d-spacing value of d(100) increased from 23.04 to 26.48 Å during the oxidation process using NaClO. Table 1 presents the relative intensities of the XRD peaks of OCP-DSG before and after the oxidation. The relative intensities of the peaks, especially the *a*-axis as demonstrated by d(100), considerably decreased. Furthermore, their FWHM considerably increased after the oxidation using NaClO. However, the relative intensities and FWHM of the peaks not related to the *a*-axis did not change by the oxidation using NaClO.

Table 1. Representative interplanar distance in OCP-DSG before and after the oxidation using NaClO.

Index	conventional-reference			OCP-DSG				NaClO oxidated			
o(hkl)	2theta	d-spacing	rel. Int.	2theta	d-spacing	rel. Int.	FWHM	2theta	d-spacing	rel. Int.	FWHM
o(100)	4.74	18.64	100.0	3.81(5)	23.14(2)	100.0	0.23	3.36(6)	26.22(9)	100.0	0.85
o(200)	9.42	9.38	8.6	7.66(7)	11.52(1)	0.2	1.68	6.42(1)	13.74(7)	0.7	1.18
o(010)	9.80	9.02	9.3	n.d.	n.d.	n.d.	n.d.	n.d.	n.d.	n.d.	n.d.
o(1-11)	16.08	5.51	3.3	15.91(5)	5.56(4)	0.2	0.31	16.39(4)	5.40(3)	1.0	2.54
o(3 21)	24.32	3.66	7.3	24.26(4)	3.66(5)	0.1	0.24	n.d.	n.d.	n.d.	n.d.
o(002)	26.08	3.41	11.4	25.94(2)	3.43(2)	1.7	0.24	25.81(6)	3.44(8)	25.5	0.24
o(221)	28.20	3.16	4.7	28.14(3)	3.16(9)	0.2	0.78	28.56(7)	3.12(2)	1.6	0.94
o(30-2)	29.22	3.05	3.1	29.34(0)	3.04(7)	0.6	0.09	29.33(1)	3.04(7)	3.9	0.11
o(5-30)	31.66	2.82	8.7	31.53(0)	2.83(5)	0.7	0.64	31.64(9)	2.82(5)	12.6	1.09
o(31 2)	32.22	2.78	3.8	32.26(3)	2.77(2)	0.6	0.77	32.17(3)	2.78(2)	21.1	1.11
o(700)	33.64	2.66	5.9	n.d.	n.d.	n.d.	n.d.	n.d.	n.d.	n.d.	n.d.
o(-711)	33.93	2.64	3.0	34.14(5)	2.62(4)	0.1	1.7	n.d.	n.d.	n.d.	n.d.

Next, spectroscopic analysis was used to assess the effect of the oxidation process using NaClO on the DSG in the interlayer of OCP. Figure 2 shows the FT–IR spectra of the samples before and after the oxidation using NaClO. Several bands corresponding to –COOH were observed around 1200–1600 cm^{-1} before the oxidation. However, there were few HPO_4 bands for *P*5 PO_4 and *P*6 PO_4, which correspond to a hydrous layer of OCP. After the oxidation, the –COOH bands disappeared, but significant carbonate bands of the B-type carbonate apatite (CO_3Ap) were observed around 1420 and 1460 cm^{-1}.[38,39] In both samples, almost no bands corresponding to independent DSG was observed. Therefore, unlike the XRD pattern analysis, the spectroscopic analysis suggested that the oxidation using NaClO converted OCP-DSG to CO_3Ap through a solid-solid phase transformation involving partial unit lattice expansion. The oxidation process using NaClO enabled DSG to be oxidized within the OCP interlayers, forming an apatite layered structure.

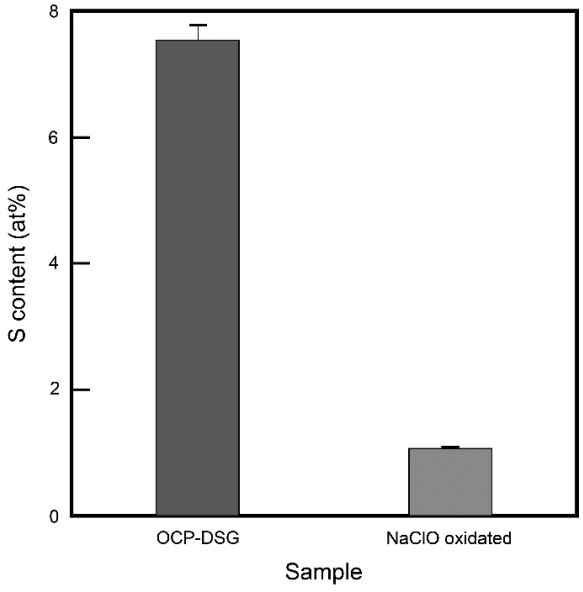

Fig. 3. S contents of OCP-DSG and NaClO oxidated OCP-DSG.

Figure 3 shows the sulfur contents of the samples before and after oxidation using NaClO measured by XRF. The sulfur content before the oxidation using NaClO was approximately 7.6 at%, which is consistent with that of the interlayer DSG, considering the crystal structure of OCP-DSG. After the oxidation using NaClO, the sulfur content dropped to approximately 1.1 at%. Based on the ICP–AES results, the Ca/P ratios of the sample before and after the oxidation using NaClO were 1.62 ± 0.02 and 1.56 ± 0.01, respectively. The possible chemical compositions of OCP-DSG before and after the oxidation using NaClO were determined to be $Ca_8H_{1.10\pm0.24}(PO_4)_{4.94\pm0.06}(DSG)_{1.14\pm0.03}\cdot nH_2O$ and $Ca_8Na_{1.14\pm0.02}H_{0.51\pm0.69}(PO_4)_{5.13\pm0.03}((COO^-)CH_2(HSO_3))_{0.12\pm0.00}(CO_3)_{1.07\pm0.04}\cdot nH_2O$, using ICP-AES, CHN, and XRF results.

The carboxyl molecules that formed a chelate with the Ca ion ($–COO^-–Ca^{2+}$ (root of OCP hydrous layer; *P*5 PO_4 conjugated site)) located at the root of the OCP hydrous layer. Consequently, this carboxyl group was considered $–COO^-$ not –COOH. Based on this reaction, we believe that carbonate molecules were attached to the surface rather than the bulk material. It was also suggested that the chemical composition of the samples without carbonate was $Ca_8Na_{1.14\pm0.02}(PO_4)_{5.13\pm0.03}(OH)_{1.75\pm0.11}\cdot nH_2O$. Considering the chemical compositions of the samples, a hydrous OCP layer (HPO_4–OH layer) was partially formed in OCP-DSG and then disappeared through oxidation with DSG. This phenomenon could be attributed to the ion-exchange process of the dicarboxylic-substituted OCP. When the dicarboxylic-substituted OCP was immersed in basic Na-containing solutions, a Ca ion exchange with Na was observed at the *P*5 PO_4 conjugated site (at the root of the hydrous layer).[27] The hydrous layer was partly reconstructed. Since the NaClO solution is a basic Na solution, a similar reaction could occur.

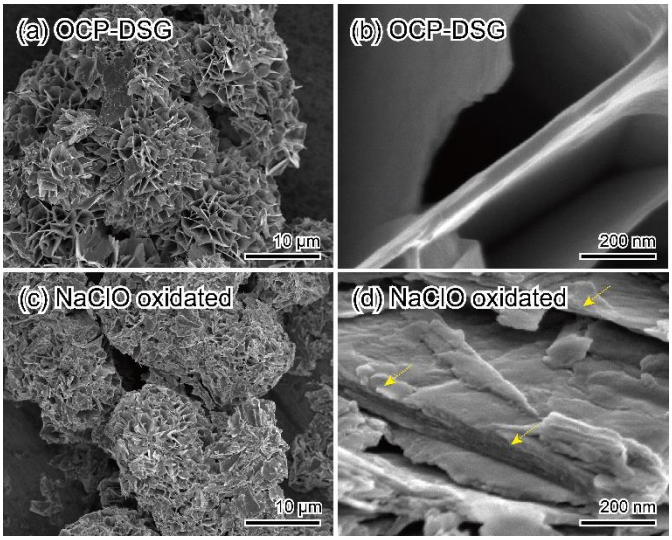

Fig. 4. SEM micrographs of OCP-DSG (a,b) and NaClO oxidated OCP-DSG (c,d). Yellow arrows indicate the in-plane grain boundaries.

Due to intercalated DSG oxidation by NaClO, an expansion of OCP layer along to *a*-axis was resulted. Note, when conventional OCP soaked into NaClO as same manner, no layer expansion phenomenon was observed. (Fig. S1)

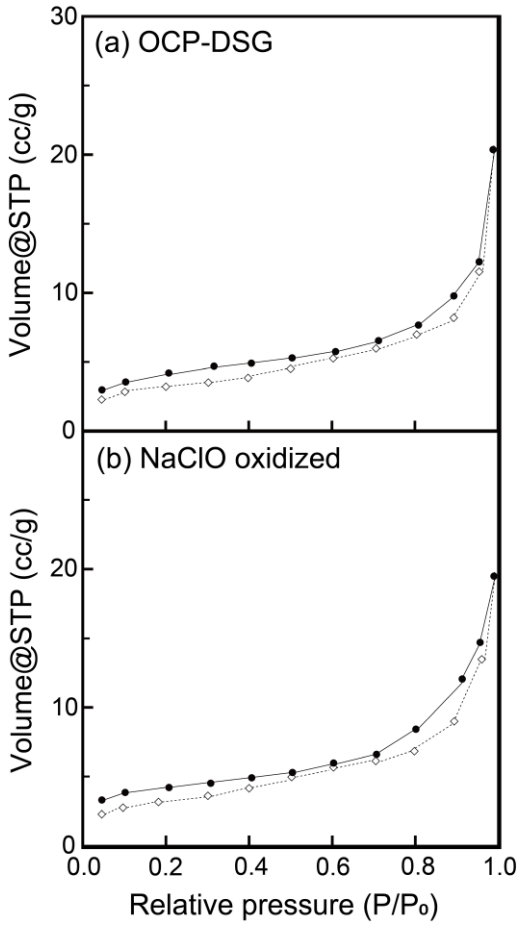

Fig. 5. Isothermal curves of (a) OCP-DSG and (b) NaClO-oxidated OCP-DSG. ● and solid black lines: adsorption. ◇ and broken black lines: desorption.

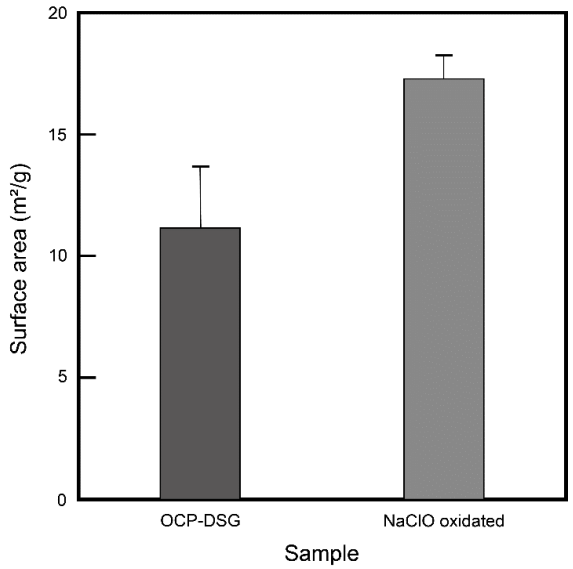

Fig. 6. Specific surface area of OCP-DSG and NaClO oxidated OCP-DSG.

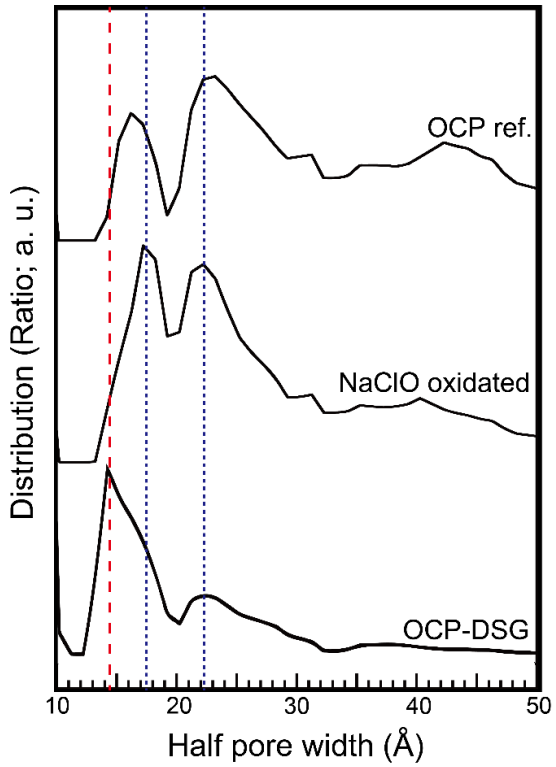

Fig. 7. Histogram of the nanopore-size distribution of OCP-DSG and NaClO- oxidated OCP-DSG.

The SEM observations provided a detailed view of the microstructures of the samples. Figure 4 shows the SEM micrographs of the samples before and after oxidation using NaClO. Before oxidation, plate-like crystals aggregated to form spherulite structures with a length of several micrometers. These crystals exhibited smooth surfaces without any cracks or holes. However, after the oxidation, the overall spherulite structures remained intact and the surfaces of the plate-like crystals became notably rougher. Despite this, there was no evidence for new crystal formation, suggesting that a dissolution–recrystallization process occurred. In addition, the thickness of the plate-like crystals considerably increased, and micro crack structures became visible on the side-by-side surfaces of the crystals, giving them the appearance of nanometer-scale laminated structures.

Figure 5 shows the BET isotherms of the samples. In contrast to OCP-DSG, the NaClO-oxidized OCP-DSG exhibited a disparity between the adsorption and desorption behaviors, particularly with the desorbed amounts of gas under high pressure being considerably smaller than the adsorbed amounts. This indicates that the gas was absorbed within the nanopores of the NaClO-oxidized OCP-DSG. thickness of the plate-like crystals increased significantly, and micro crack structures became visible on the side-by-side surfaces of the crystals, giving them the appearance of nanometer-scale laminated structures.

Figure 6 highlights the specific surface areas of the samples, as measured using the BET method. Before and after NaClO oxidation, the surface areas of OCP-DSG were 11.2 ± 2.6 m^2/g and 17.3 ± 1.0 m^2/g, respectively, suggesting only a slight increase in the samples' surface areas post oxidation. To further assess the surface area, we evaluated the pore size distributions of the samples to understand how pore structures are formed within the OCP structures. Figure 7 shows the pore size distributions of the samples before and after NaClO oxidation. A monomodal pore distribution of 14.2 Å was observed at the local maximum value before NaClO oxidation. After NaClO oxidation, the pore distribution of the sample became bimodal, with the local maximum values of the distribution shifting to 17.2 Å and 22.1 Å. The 17.2 Å pore value nearly coincided with the length of the *a*-axis unit lattice of OCP-DSG after NaClO oxidation, excluding the length of the apatite layer. Therefore, we can suggest that these pore structures were caused by the disappearance of the DSG layer and expansion of the OCP interlayer.

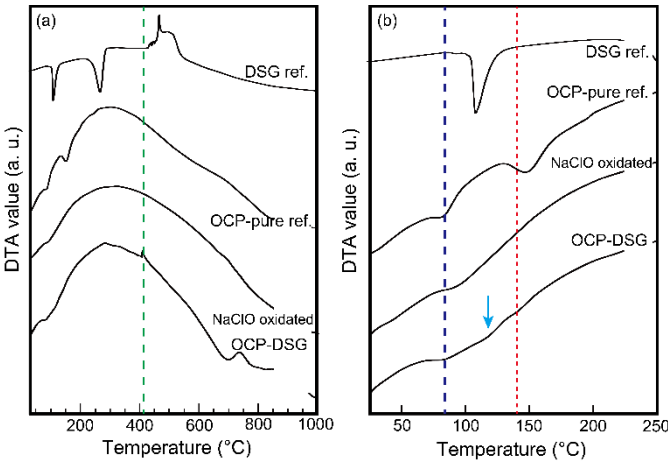

Fig. 8. DTA curves of OCP-DSG and NaClO-oxidized OCP-DSG: (a) Wide range. The green broken line indicates the DSG detaching from the OCP-DSG surface. (b) Hydrous layer range. The blue and red broken lines indicate the moisture detaching from the surface and the temperature of the collapse of the hydrous layer of OCP-DSG, respectively. The light blue arrow indicates the collapse of the dicarboxylic acid intercalation structure.[41]

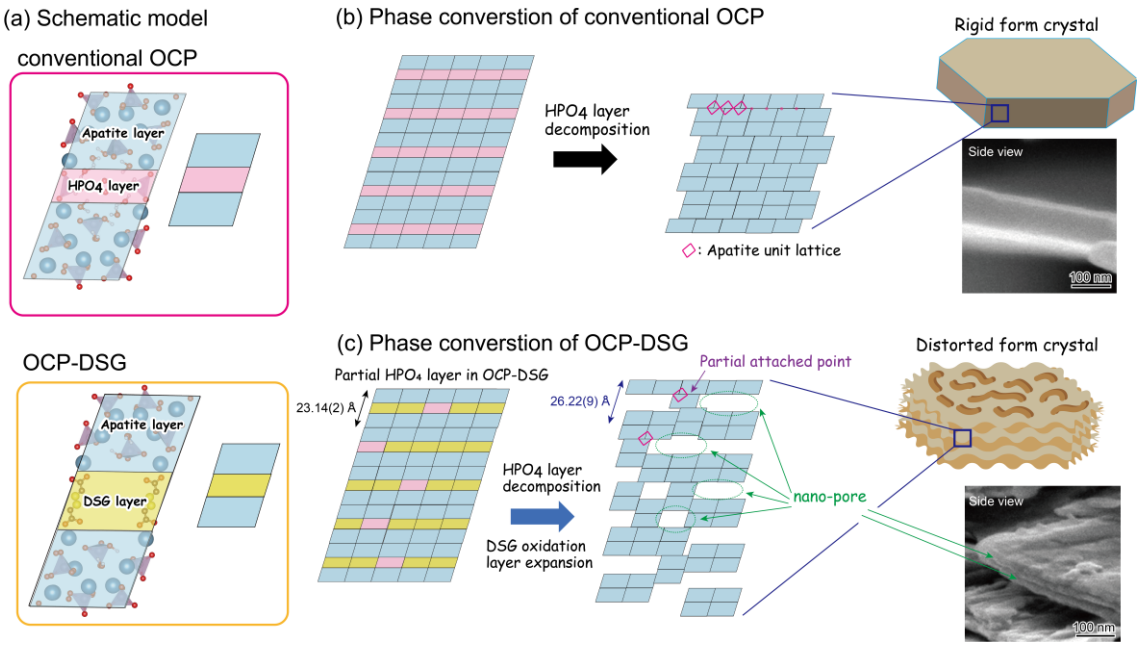

Scheme 2. Schematic of the nanopore formation process of OCP-DSG through the NaClO-forced oxidation process. (a) Unit lattice of conventional OCP and OCP-DSG and their deformations. (b) Phase conversion process for conventional OCP. (c) Phase conversion process for OCP-DSG.

The samples were thermally evaluated to explore the relationship between the DSG oxidation and the decomposition of the hydrous layer in the interlayer of the OCP unit lattice. Figure 8 shows the differential thermal analysis (DTA) curves of the samples. Past studies have shown that the hydrous layer of OCP decomposes at around 150°C.[21,40] This trend was also observed in dicarboxylic-acid-intercalated OCP; however, several peaks were observed at slightly lower temperatures. These peaks were associated with the decomposition of the dicarboxylic acid region.[34,41] Similar to other dicarboxylic acid-intercalated OCPs, the decomposition of the dicarboxylic acid structure and hydrous layer of OCP-DSG occurred below 150°C. Moreover, the decomposition temperature of the hydrous layer of OCP-DSG was slightly lower than that of pure OCP. With the increase in the temperature, the intercalated DSG decomposed and/or detached from the OCP unit lattice at approximately 400°C. However, for the oxidation sample, only minimal decomposition of the hydrous layers and dicarboxylic acid intercalation was observed. Thus, it can be suggested that, through the oxidation process using NaClO, OCP-DSG retained a few hydrous layers and intercalated structures while preserving its layered structure.

The results indicate that the forced oxidation process of OCP-DSG using NaClO caused the decomposition of the substituted DSG in the OCP interlayer during the phase transformation process from OCP to apatite via solid–solid phase conversion. Consequently, the OCP layers exhibited an expansion while their structure was maintained. Furthermore, the FT–IR measurements revealed that after oxidation using NaClO, only a small part of the hydrous layer of OCP (HPO_4–OH layer) was preserved and the samples were identified as CO_3Ap. This process can be essentially considered a phase conversion process of OCP to apatite, but with a partially expanded crystal lattice.

This phenomenon is summarized in Scheme 2. Essentially, this reaction can be described as the decomposition of the hydrous layer of OCP. However, the oxidation of the –S–S– bond of the intercalated DSG caused the OCP interlayer to expand beyond the layer fusion process during phase conversion. Consequently, nanopores were formed in the samples. Nevertheless, the partially retained HPO_4 layers of OCP-DSG were dehydrated after the phase conversion process. When OCP-DSG was immersed in an aqueous solution, it was converted into a conventional apatite (Fig. S2). Thus, OCP-DSG was converted into CO_3Ap with a layered structure derived from OCP through oxidation using NaClO. This process is distinct from other ion-exchange processes between the OCP interlayers, such as NH_4 to Na,[31,32] because in the current case, the layered structure was significantly altered.

Although previous studies have indicated that various molecules can be intercalated into the OCP interlayers, maintaining their stability in OCP unit lattices has proven to be challenging, particularly in applications such as drug delivery systems (DDSs). For instance, typically, intercalated dicarboxylic acid molecules are easily detached during phase conversion.[29,30,33] Based on this process, nanopores could be introduced into OCP (or OCP-based materials). For various medical applications, the nanopores containing calcium phosphate could serve as drug carriers for DDS devices. Therefore, the method proposed in this study could greatly contribute to new medical applications and enhance QOL.

This study provides a different understanding than the previous one of the OCP phase conversion process, which was believed to only involve a shrinkage process either mediated by an aqueous solution or through thermal decomposition.[21,34,35,40,42-44] Here, we clarified that the forced oxidation process of the intercalated molecules between OCP interlayers can induce expansion, resulting in the formation of nanoporous structures. In the case of OCP, the remaining HPO_4 layers contribute to the nanopore formation.

Conclusions

In conclusion, we demonstrated that forced oxidation using NaClO can facilitate the decomposition of the substituted DSG within the OCP interlayers. After the oxidation process using NaClO, a significant expansion of the interlayer within the OCP unit lattice and a phase transition into B-type CO_3Ap with a partially expanded layered structure were observed. The overall process resulted in the formation of a sheet-like nanoporous structure within the apatite interlayer.

Author Contributions

Y.S. and M.H. conceived and designed the experiments; Y.S. and E.Y. performed the experiments and analysed the data; Y.S. and M.H. wrote the manuscript; and Y.S., E.Y. and M.H. discussed the experiments and the manuscript.

Conflicts of interest

There are no conflicts to declare.

Acknowledgements

We thank Dr. T. Nakanishi, RIST Kagawa, Japan, for FT-IR measurement. This study is financially supported by AMED SeedsH program (Keio Univ.) Grant Number H424TS, AMED SeedsA program (Keio Univ.) Grant Number A424TR, Kazuchika Okura Memorial Foundation 2022FY grant-in-aid and, JST-CREST, Grant number: JPMJCR22L5.

Notes and references

1 T. J. Pinnavaia, *Science*, 1983, **220**, 365.
2 V. Nicolosi, M. Chhowalla, M.G. Kanatzidis, M.S. Strano, J.N. Coleman, *Science*, 2013, **340**, 1226419.
3 R. Sousa, J. Jouin, O. Masson, F. Remondiere, A. Lemarchand, M. Colas, P. Thomas, J. Lameira, G.N.T. Bastos, A.B. Lima, J.L.M. Nascimento, M. Anicete-Santos, W.R. Monteiro, C.N. Alves, *J. Am. Ceram. Soc.*, 2017, **100**, 2712.
4 E.P. Komarala, S. Doshi, S. Thiyagarajan, M. Aslam, D. Bahadur, *New J. Chem.*, 2018, **42**, 129.
5 E. Cruz Jr., E.J. Broker Jr., B.M. Mosby, *Dalton Trans.*, 2020, **49**, 3841.
6 L. Wang, G.H. Nancollas, *Chem. Rev.*, 2008, **108**, 4628.
7 S.V. Dorozhkin, *Biomater.*, 2010, **31**, 1465.
8 S.V. Dorozhkin, *Materials*, 2009, **2**, 399.
9 O. Suzuki, Y. Shiwaku, R. Hamai, *Dent. Mater. J.*, 2020, **39**, 187.
10 K. Ishikawa, *J. Ceram. Soc. Jpn.*, 2019, **127**, 595.
11 R.Z. LeGeros, *Chem. Rev.*, 2008, **108**, 4742.
12 K. Kaneda, T. Mizugaki, *Energy Environ. Sci.*, 2009, **2**, 655.
13 M.R. Elahifard, S. Rahimnejad, S. Haghighi, M.R. Gholami, *J. Am. Chem. Soc.*, 2007, **129**, 9552.
14 W.E. Brown, J.P. Smith, J.R. Lehr, A.W. Frazier, *Nature*, 1962, **196**, 1050.
15 E. Davies, M.J. Duer, S.E. Ashbrook, J.M. Griffin, *J. Am. Chem. Soc.*, 2012, **134**, 12508.
16 T.W.T. Tsai, F.-C. Chou, Y.-H. Tseng, J.C.C. Chan, *Phys. Chem. Chem. Phys.*, 2010, **12**, 6692.
17 Y. Sugiura, *J. Ceram. Soc. Jpn.*, 2022, **130**, 369.
18 A. Ressler, I. Ivanišević, A. Žužić, N. Somers, *Ceram. Int.*, 2022, **48**, 8838.
19 M. Markovic, B.O. Fowler, W.E. Brown, *Chem. Mater.*, 1993, **5**, 1406.
20 H. Shi, F. He, J. Ye, *J. Mater. Chem. B*, 2016, **4**, 1712.
21 E. Boanini, M. Gazzano, K. Rubini, A. Bigi, *Cryst. Growth Des.*, 2010, **10**, 3612.
22 Y. Sugiura, Y. Saito, T. Endo, Y. Makita, *Cryst. Growth Des.*, 2019, **19**, 4162.
23 I. Yamada, M. Tagaya, *Colloid Interf. Sci. Comm.*, 2019, **30**, 100182.
24 Y. Sugiura, Y. Makita, *Chem. Lett.*, 2018, **47**, 1371.
25 Y. Sugiura, Y. Makita, *Chem. Lett.*, 2019, **48**, 1304.
26 Y. Sugiura, K. Niitsu, Y. Saito, T. Endo, M. Horie. *RSC Adv.*, 2021, **11**, 12330.
27 Y. Sugiura, F. Ono, M. Nohara, R. Horino, K. Kutara, T. Kanda, K. Oowada, M. Horie, Y. Makita, *Mater. Today Comm.*, 2022, **30**, 103130.
28 Y. Sugiura, F. Ono, M. Nohara, A. Takechi, K. Kutara, T. Kanda, Y. Saito, E. Yamada, K. Oowada, T. Endo, M. Horie, Y. Makita, *Materialia*, 2023, **28**, 101771.
29 T. Yokoi, T. Goto, S. Kitaoka, *Chem. Lett.*, 2019, **48**, 855.
30 Y. Sugiura, Y. Makita, *J. Cryst. Growth*, 2022, **583**, 136545.
31 Y. Sugiura, Y. Makita, M. Horie, *RSC Adv.*, 2021, **11**, 39503.
32 Y. Sugiura, Y. Makita, *Dalton Trans.*, 2019, **48**, 1386.
33 T. Yokoi, T. Goto, T. Kato, S. Takahashi, J. Nakamura, T. Sekino, C. Ohtsuki, M. Kawashita, *Bull. Chem. Soc. Jpn.*, 2020, **93**, 701.
34 Y.-H. Tseng, C.-Y. Mou, J.C.C. Chan, *J. Am. Chem. Soc.*, 2006, **128**, 6909.
35 Y. Sugiura, M. Horie, *Ceram. Int.*, 2021, **47**, 25614.
36 A. LeBail, H. Duroy, J.L. Fourquet, *Mater. Res. Bull.* 1988, **23**, 447.
37 S. Brunauer, P.H. Emmett, E. Teller, *J. Am. Chem. Soc.*, 1938, **60**, 309.
38 R.Z. LeGeros, O.R. Trautz, E. Klein, J.P. LeGeros, *Exp. A*, 1969, **15**, 1.
39 C. Rey, B. Collins, T. Goehl, I.R. Dickson, M.J. Glimcher, *Calcif. Tissue Int.*, 1989, **45**, 157.
40 D.G.A. Nelson and J.D. McLean, *Calcif. Tissue Int.*, 1984, **36**, 219.
41 Y. Sugiura, Y. Makita, *J. Solid State Chem.*, 2019, **279**, 120923.
42 H. Monma, *Gypsum Lime*, 1990, **229**, 396.
43 M. Kamitakahara, N. Ito, S. Murakami, N. Watanabe, K. Ioku, *J. Ceram. Soc. Jpn.*, 2009, **117**, 385.
44 N. Ito, M. Kamitakahara, M. Yoshimura, K. Ioku, *Mater. Sci. Eng. C*, 2014, **40**, 121.
45 L.I. Jong and N.L. Abbott, *Langmuir*, 2000, **16**, 5553.
46 L.A. Oparina, G.Y. Perchuzov, L.A. Novgorodskaya, V.I. Bolmosov and A.M. Stepanov, *J. Appl. Chem. USSR*, 1986, **59**, 1184.
47 B.O. Fowler, M. Markovic, W.E. Brown, *Chem. Mater.*, 1993, **5**, 1417.
48 E.E. Berry, C.B. Baddiel, *Spectrochim. Acta*, 1967, **23A**, 1781.